Nanoscale Advances

ROYAL SOCIETY OF CHEMISTRY

PAPER

Cite this: *Nanoscale Adv.*, 2023, **5**, 4470

Stabilization and adiabatic control of antiferromagnetically coupled skyrmions without the topological Hall effect†

Rawana Yagan, [a] Arash Mousavi Cheghabouri[a] and Mehmet C. Onbasli *[ab]

Synthetic antiferromagnetically coupled (SAF) multilayers provide different physics of stabilizing skyrmions while eliminating the topological Hall effect (THE), enabling efficient and stable control. The effects of material parameters, external current drive, and a magnetic field on the skyrmion equilibrium and propagation characteristics are largely unresolved. Here, we present a computational and theoretical demonstration of the large window of material parameters that stabilize SAF skyrmions determined by saturation magnetization, uniaxial anisotropy, and Dzyaloshinskii–Moriya interaction. Current-driven SAF skyrmion velocities reach ~200 m s^{-1} without the THE. The SAF velocities are about 3–10 times greater than the typical ferromagnetic skyrmion velocities. The current densities needed for driving SAF skyrmions could be reduced to 10^8 A m^{-2}, while 10^{11} A m^{-2} or above is needed for ferromagnetic skyrmions. By reducing the SAF skyrmion drive current by 3 orders, Joule heating is reduced by 6 orders of magnitude. These results pave the way for new SAF interfaces with improved equilibrium, dynamics, and power savings in THE-free skyrmionics.

Received 13th April 2023
Accepted 26th July 2023

DOI: 10.1039/d3na00236e

rsc.li/nanoscale-advances

Skyrmions are chiral topologically protected quasi-particles that exist in chiral magnets.[1,2] These quasi-particles entail rich materials physics such as competing short- or long-range magnetic order in both non-centrosymmetric and symmetric lattices,[3,4] lower order vortex or antivortex topologies such as (anti)merons,[5] coupling with other quasi-particles such as non-Abelian anyons,[6] and ferroelectric or thermal control in 2D van der Waals heterostructures.[7,8] In addition, great interest is directed toward developing skyrmion-based memory and logic devices for next-generation applications that require fast and energy-efficient operations.[9,10] Their nanoscale dimensions enable high-density and low-power nonvolatile devices. For the low and room temperature stabilization and manipulation of skyrmions for such applications, new ferromagnetic (FM) and antiferromagnetic (AFM) thin films and multilayers with unique combinations of magnetic material properties are needed.[11,12]

Ferromagnetic (FM) thin films can stabilize skyrmions for the optimal combinations of saturation magnetization (M_{sat}), uniaxial anisotropy (K_u), and Dzyaloshinskii–Moriya Interaction (DMI) terms at low and room temperatures.[13] Their current pulse-driven control hints[14,15] that these skyrmions might be applied in racetrack memories.[16,17] Nevertheless, several limitations of FM skyrmions have been observed, such as the topological Hall effect (THE), skyrmion pinning sites, and a narrow window of stability under external magnetic fields and drive currents, and strong dependence on temperature. To eliminate these shortcomings, synthetic antiferromagnetically coupled (SAF) multilayers could be used for stabilizing skyrmions while eliminating the topological Hall effect (THE), achieving faster, more efficient, and more stable current-driven propagation. To obtain these advantageous characteristics, the effects of material and external drive conditions on the SAF skyrmion equilibrium and propagation need to be understood.

Topologically non-trivial spin textures such as SAF skyrmions and domain walls have been previously proposed for magnetic tunability for applications.[18–20] In SAF structures, as in Fig. 1(a), the two thin FM films couple antiferromagnetically through the non-magnetic spacer by interlayer exchange interaction (ILE), known as the Ruderman–Kittel–Kasuya–Yoshida (RKKY) interaction.[21,22] This effect has been shown to enhance the stability and the velocity of SAF skyrmions.[23] Previous studies suggested that the chiral SAF structures help stabilize skyrmions, eliminate the THE and might enable efficient and stable control.[24,25] The theory of ferromagnetic skyrmions has been established,[26,27] but the effects of material parameters, external current drive, and a magnetic field on the SAF skyrmion equilibrium and propagation characteristics have not been fully understood. A complete understanding of such characteristics should enable design of SAF skyrmion physics with low current requirements and high velocities. In addition, the effect of material imperfections such as polycrystallinity and side wall

[a]*Department of Electrical and Electronics Engineering, Koç University, Sarıyer, Istanbul 34450, Turkey. E-mail: monbasli@ku.edu.tr*

[b]*Department of Physics, Koç University, Sarıyer, Istanbul 34450, Turkey*

† Electronic supplementary information (ESI) available: The data and the part of the code used for the models. See DOI: https://doi.org/10.1039/d3na00236e

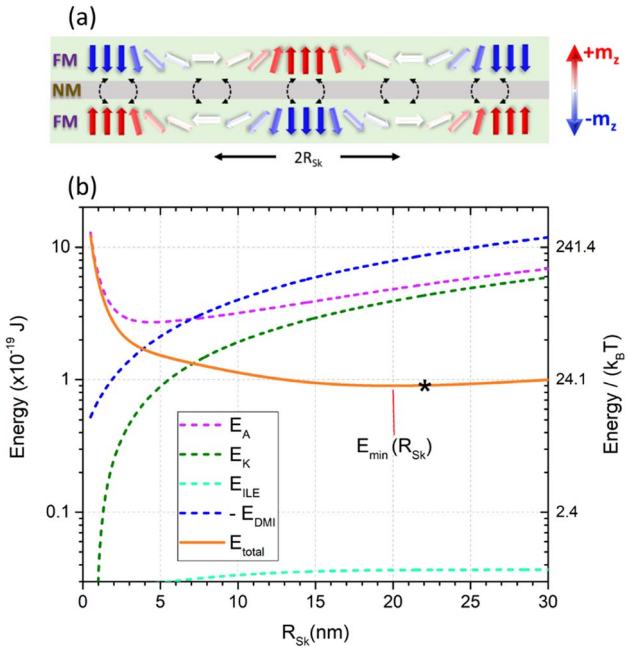

Fig. 1 Stability of skyrmions in SAF. (a) Simulated structure and visualization of a SAF skyrmion. The black arrows over the nonmagnetic layer show the interlayer exchange coupling mainly through RKKY interactions. (b) The calculated total energy of the skyrmion in a single FM layer and its energy terms as functions of its radius. Material parameters are from ref. 35: $M_{sat} = 954 \times 10^3$ A m^{-1}, $A = 10 \times 10^{-12}$ J m^{-1}, $K_u = 0.85 \times 10^6$ J m^{-3}, $D_{ind} = 2.0 \times 10^{-3}$ J m^{-2}, $J_{int} = -0.13 \times 10^{-3}$ J m^{-2}, damping $\alpha = 0.1$, and the FM layer thickness $d = 1$ nm.

roughness as well as temperature effects on the advantages of SAF skyrmions need to be investigated. Thus, a comprehensive theory and modelling study is necessary to explain the SAF skyrmion physics. Such a study could help explain the dominant material and control parameters and regimes that could help design stable, efficient, fast, and THE-free devices.

In this paper, we investigate and stabilize SAF skyrmions in FM/NM (nonmagnetic)/FM layers. We developed and ran micromagnetic[28] and semi-analytical models to show that the intrinsic layer magnetic properties M_{sat}, K_u and interfacial DMI constant (D_{ind}) play a central role in the stability, energy cost and skyrmion size control. The interlayer exchange coupling effect, which mainly depends on the interaction coefficient J_{int}, contributes a weaker but an essential term in eliminating the THE. J_{int} helps robust stabilization and prevents skyrmion decoupling under external magnetic fields and current densities perpendicular to the film plane (CPP). We investigated the effect of spin–orbit torque-driven current control in the CPP configuration, which allows for stable SAF skyrmion propagation over 3 orders of magnitude current densities (10^8 to 10^{11} A m^{-2}). The current densities needed for driving SAF skyrmions could be reduced to 10^8 A m^{-2} (adiabatic limit), which is up to 3 orders of magnitude lower than the currents needed for ferromagnetic skyrmions (10^{11} A m^{-2} or above).[29] Thus, Joule heating might be reduced by 6 orders of magnitude. The current-driven SAF skyrmion velocities reach ~200 m s^{-1} without the THE, which is about an order of magnitude greater than the ferromagnetic skyrmion velocities.[30] Earlier studies[25] showed high SAF skyrmion velocities exceeding 1000 m s^{-1} at 3×10^8 A cm^{-2} (or 3×10^{12} A m^{-2}), but in our case, we report current density requirements of 10^8 to 10^{11} A m^{-2} for ~200 m s^{-1}, where 1–3 orders of lower current densities in our study might benefit device applications.

Significant polycrystallinity or material parameter variations over each nanoscale grain have been found to cause SAF skyrmion pinning and change the current needed for SAF skyrmion propagation. Thus, uniform material characteristics are necessary for experiments. Side wall roughness does not significantly affect the SAF skyrmion stability or propagation. Stabilizing SAF skyrmions at higher temperatures required larger uniaxial anisotropy constants. These results and the semi-analytical model here provide insights into new SAF interfaces for improved equilibrium and dynamics of skyrmions without the THE. Thus, THE-free long-distance propagation and operation of skyrmions on chip without undergoing deflection or significant heating might become feasible.

Our modeling approach identified the effects of polycrystallinity that previous studies did not uncover.[31,32] Earlier studies used hysteresis loop models for coercivity and remanence for arrays of nickel nanowires[31] but did not investigate current drive, skyrmion formation or stability or antiferromagnetic coupling. In our case, we studied the SAF skyrmion pair equilibria under magnetic compensation and current drive and material imperfections.

In the next section, we first describe the stabilization of SAF skyrmions using both micromagnetic modelling and semi-analytical energy minimization. Then, we present the dependence of the SAF skyrmion stability and radius on the intrinsic magnetic layer parameters (M_{sat}, D_{ind}, and K_u), the interlayer exchange (J_{int}), and the applied external magnetic field and current density. Next, we discuss and identify the main parameters that must be used for SAF skyrmion stabilization and adiabatic drive with no or negligible THE. We compare our results with those of previous studies on the elimination of the THE and highlight that THE-free SAF skyrmions can be driven with current densities over several orders of magnitude.

Results

SAF and stabilization of AFM coupled skyrmions

An SAF skyrmion consists of two ferromagnetic skyrmions coupled antiferromagnetically through a FM/NM/FM heterostructure. The magnetization of each FM layer's skyrmion core is opposite to the film plane and has opposite topological charge with respect to their antiferromagnetically coupled skyrmion counterpart as shown in Fig. 1(a).

For each layer, the skyrmion and its related analytical energy approximation expressions are adapted from the FM skyrmion system of equations.[27] In each layer, the moment is represented by the normalized unit magnetization vector, $\mathbf{m} = (\sin\theta\cos\varphi, \sin\theta\sin\varphi, \cos\theta)$, in spherical coordinates and described by the polar and azimuthal angles, θ and φ, respectively. The domain wall in a skyrmion, as shown in Fig. 1(a), is defined as the transition region from the oppositely polarized spins (from red to blue)

within a skyrmion. **m** is assumed to be uniform across the layer thickness (φ is constant) and has a constant saturation magnetization M_{sat}. φ is the angle between the domain wall magnetic moments and the radial direction (r) and $\theta(\varrho,\rho)$ is the skyrmion profile modeled by the 360° domain wall proposed by Braun:[33]

$$\theta(\varrho,\rho) = 2\left(\tan^{-1}\left(e^{\varrho-\rho}\right) + \tan^{-1}\left(e^{\varrho+\rho}\right)\right) - \frac{(N+1)\pi}{2}, \quad (1)$$

where $\rho = \frac{R_{Sk}}{w}$ and $\varrho = \frac{r}{w}$. R_{Sk} is the skyrmion radius, w is the skyrmion domain wall width and N is the skyrmion core (= 1 here since skyrmion core moments point upwards for the top FM layer).

The total energy of a single FM layer within the SAF heterostructure consists of the energy terms that are driven by the intrinsic, interaction and external bias magnetic energy terms: demagnetizing field energy, Heisenberg exchange E_A, effective anisotropy E_K, DMI E_{DMI}, interlayer exchange E_{ILE} and Zeeman energy E_Z:

$$E_{tot} = E_A + E_K + E_{DMI} + E_{ILE} + E_Z \quad (2)$$

Each magnetic anisotropy energy term shown below and in eqn (2) is calculated for each FM layer separately:

$$E_A = 2\pi Ad\left(2\rho + \frac{2}{\rho} + 1.93(\rho - 0.65)\, e^{(-1.43(\rho-0.65))}\right), \quad (3)$$

$$E_K = 2\pi Kdw^2\left(2\rho - \frac{1}{3}e^{-\frac{\rho}{\sqrt{2}}}\right) \quad (4)$$

$$E_{DMI} = -2\pi dw(D_{ind}\cos\phi)\left(\pi\rho + \frac{1}{2}e^{-\rho}\right), \quad (5)$$

$$E_{ILE} = -2\pi J_{int}dw(5.005\text{–}2.149\, e^{-0.93\rho}). \quad (6)$$

A is the exchange stiffness constant.

The demagnetization field energy is included in the E_K term using:

$$K = K_u - \frac{1}{2}\mu_o {M_{sat}}^2 \quad (7)$$

as the shape anisotropy, where K_u is the perpendicular (uniaxial) magnetocrystalline anisotropy and μ_o is the magnetic permeability of vacuum. This approximation is acceptable in the case where the layer thickness d is much smaller than the skyrmion radius, R_{Sk}.[26,27] Here, we assume to have interfacial DMI since Néel skyrmions (φ = 0, domain moments are pointing outward) are present in the SAF, so D_{ind} is the interaction constant of the interface. $\mu_o H_z$ is the applied external out-of-plane magnetic field. The ILE functional, E_{ILE}, was solved numerically from the definition in ref. 34 and approximated with the RKKY interaction constant J_{int}, which accounts for the interlayer exchange energy constant.

In these calculations, E_A, E_k, and E_{DMI} are determined by each layer's intrinsic magnetic parameters and geometry. E_{ILE} is the term that couples the FM skyrmions antiferromagnetically through the nonmagnetic layer and depends on the geometry (thickness), the interface characteristics, and ρ, whose equilibrium value is affected by all the other magnetic energy terms. E_Z is the external magnetic field bias control term for stabilizing the SAF skyrmion. In the semi-analytical model, the thin film aspect ratio is assumed.

We first find the equilibrium skyrmion radii using both self-consistent solutions of the approximations given in eqn (1)–(7) and using numerical micromagnetic modelling of the Landau–Lifshitz–Gilbert equation. These two models help identify the key energy terms and the material parameters that strongly affect the SAF skyrmion stability.

The equilibrium radius of the SAF skyrmion for an experimentally relevant[35] set of material parameters is found by minimizing the total magnetic anisotropy energy with respect to the coupled SAF skyrmion radius R_{Sk}. Fig. 1(b) shows the dependence of the radius of the SAF skyrmion on one of the FM/NM interfaces to the total effective magnetic energy and the different energy terms (E_A, E_K, E_{DMI}, and E_{ILE}) contributing to the equilibrium, as shown in eqn (3)–(7) of our semi-analytical model. This curve is identical for the skyrmion stabilized at the opposite interface of the FM/NM/FM trilayer. The star on the total energy curve corresponds to the calculated equilibrium radius and energy using a LLG-based micromagnetic model. Both numerical micromagnetic models (R_{eq} = 22 nm) and the semi-analytical model (R_{eq} = 19.99 nm) yield almost identical equilibrium skyrmion radii for the SAF trilayer system.

Effect of material parameters on SAF skyrmion stability

We now investigate the stability and equilibrium radii of the SAF skyrmions using LLG-based micromagnetic models as functions of different M_{sat}, D_{ind} (DMI) and K_u values.

Fig. 2(a) shows the effect of the saturation magnetization and demagnetization field on the radius of the skyrmion along the top FM/NM surface. The energy terms for both top and bottom FM/NM interfaces include the uniaxial anisotropy, DMI, Heisenberg exchange, and interlayer exchange; therefore, the resulting plots for the skyrmions at both interfaces are identical. R_{Sk} shows a linear scaling trend with the increase in M_{sat} until 950 kA m^{-1}, and then the radius scales exponentially with M_{sat} as the demagnetization energy starts dominating the total magnetic energy of the skyrmions. This effect is also mirrored in the second FM layer (not shown).

We next calculated the phase diagram of R_{Sk} as a function of M_{sat} and the uniaxial anisotropy constant, K_u, shown in Fig. 2(b). On the top left corner of the phase diagram (low K_u and high M_{sat}), a transition from a labyrinth domain structure (shown in the inset figure) is observed and skyrmions cannot be stabilized. As K_u is increased, the skyrmion radii decrease from 38 to 1.25 nm. With further increase in K_u and reduction in M_{sat}, skyrmions would be expected to shrink further but since the micromagnetic model cell size cannot be smaller than the lattice constant of cobalt, smaller skyrmion size regions have been excluded from the phase diagram. The lower right-hand corner of the phase diagram (gray area; high K_u and low M_{sat}) reaches the minimum allowed mesh size of the micromagnetic model (exchange length > minimum cell size > lattice constant of cobalt). No result is shown for this

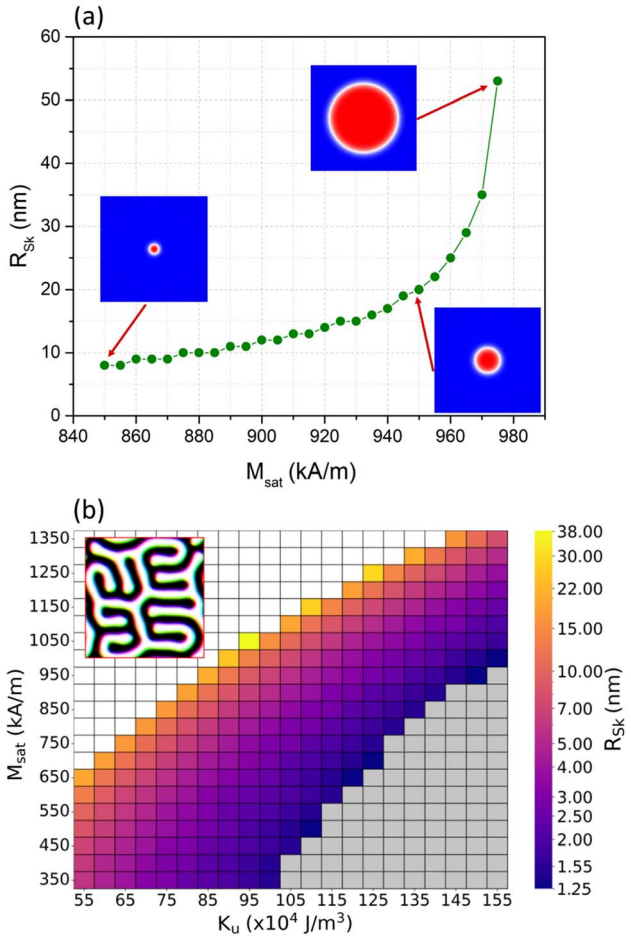

Fig. 2 Magnetostatic and anisotropy field effect on the skyrmion stability. (a) The skyrmion radius R_{Sk} as a function of the saturation magnetization (M_{sat}) of the SAF system. (b) Phase diagram of the relaxation radius as a function of M_{sat} and K_u. In both (a) and (b), the material parameters are kept the same as before ($M_{sat} = 954 \times 10^3$ A m^{-1}, $A = 10 \times 10^{-12}$ J m^{-1}, $K_u = 0.85 \times 10^6$ J m^{-3}, $D_{ind} = 2.0 \times 10^{-3}$ J m^{-2} and $\alpha = 0.1$) except for the swept constants.

region since the LLG model cannot account for the atomic scale interactions. Higher K_u shrinks the skyrmion radius, while greater M_{sat} enlarges the skyrmion.

Fig. 3 shows the effect of interfacial Dzyaloshinskii–Moriya interaction strength, D_{ind}, and uniaxial anisotropy K_u on the relaxed and equilibrated skyrmion size. Increasing K_u for a fixed D_{ind} equilibrates the skyrmions at lower radii ($R_{eq} < 5$ nm). For a fixed K_u, the equilibrium skyrmion radii increase to 15 to 30 nm with higher D_{ind} values. For low K_u and high D_{ind} values, the skyrmions are not stable and labyrinth domains form as shown in the inset of the figure. The gray region does not include any results as in Fig. 2(b), since the required cell size approaches the lattice constant.

Effect of external control fields on SAF skyrmion stability

The stability of SAF skyrmions relies on the intrinsic material parameters as well as the extrinsic control conditions including the magnetic field ($B_z = \mu_o H_z$) and the current density. To elucidate the effect of an external magnetic field on the SAF

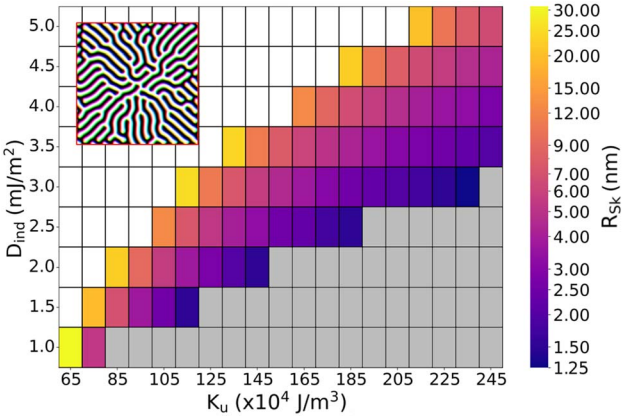

Fig. 3 DMI and uniaxial anisotropy constant dependence of skyrmion dimensions. The equilibrium phase diagram for both top and bottom SAF skyrmion radii as functions of the DMI constant (D_{ind}) and uniaxial anisotropy constant (K_u) shows a window of stable skyrmion radii between 1.25 and 30 nm.

skyrmion stability and coupling, the approximated Zeeman energy term shown[27] in eqn (8) is added to the total energy terms (eqn (2)) for both top and bottom skyrmions calculated using the micromagnetic solver.

$$E_Z = 2\pi\mu_o H_z M_{sat} dw^2 \left(\rho^2 + \frac{\pi^2}{12} - 0.42e^{-\rho^2}\right), \quad (8)$$

In Fig. 4(a), the equilibrium skyrmion radii for both the top and the bottom interfaces have been calculated and plotted as functions of the applied out of plane magnetic field. Because the bottom skyrmion experiences H_z in the opposite direction as the top skyrmion, the energy term for the bottom skyrmion has the opposite sign in its total energy. Thus, the magnetic field scaling profiles of the skyrmion radii are different due to the different Zeeman energy term signs for the two skyrmions. At low fields, the radii of the coupled SAF skyrmions are the same. For $B_z > 10$ mT, the mirror symmetry of the skyrmions gets broken and beyond 50 mT, the geometric difference starts diverging.

Because these skyrmions are coupled with each other through the ILE, the skyrmion scaling with the applied field and the ILE coefficient needs to be understood. For this purpose, we calculated and plotted the radii of the bottom skyrmion as functions of J_{int} (interlayer exchange coupling coefficient) and the applied field B_z in Fig. 4(b).

Finally, we investigated the effect of current density on the dynamical stability and velocity of the SAF skyrmions. We studied this effect by applying current-induced spin–orbit torque (SOT) perpendicular-to-plane (CPP) to the SAF structure (eqn (11) in the Methods) that allows the skyrmion pair to travel in the in-plane direction ($+x$). In Fig. 5(a), we apply a current density of $J_e = 2.5 \times 10^{11}$ A m^{-2} from left to right to push the skyrmion pair along the structure with a spin Hall angle $\theta_{Hall} = 0.25$.[35] We observe that for the lower applied field, the SAF skyrmion with the higher ILE coupling constant J_{int} experiences higher velocity; however at a critical B_z field of near 80 mT, all curves show the same velocity, and the order is reversed. The smallest J_{int} curve gives the highest skyrmion velocity at higher

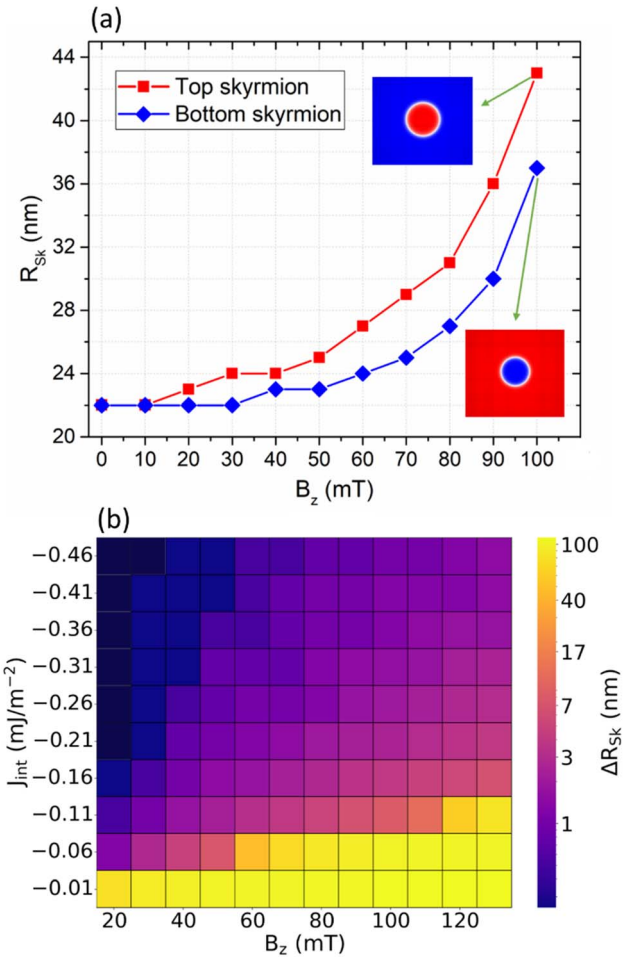

Fig. 4 Decoupling SAF skyrmion pairs under external magnetic fields and weak interlayer exchange. (a) Effect of an external magnetic field (Zeeman energy) on the stabilized top and bottom skyrmion radii ($J_{int} = -0.13$ J m^{-2}). Red indicates the magnetization pointing in the $+z$ direction as the external field B_z while blue indicates the magnetization pointing in the opposite direction along $-z$. (b) J_{int} and B_z effects on the skyrmion radius. The black region indicates $\Delta R_{Sk} = 0$ nm (no difference).

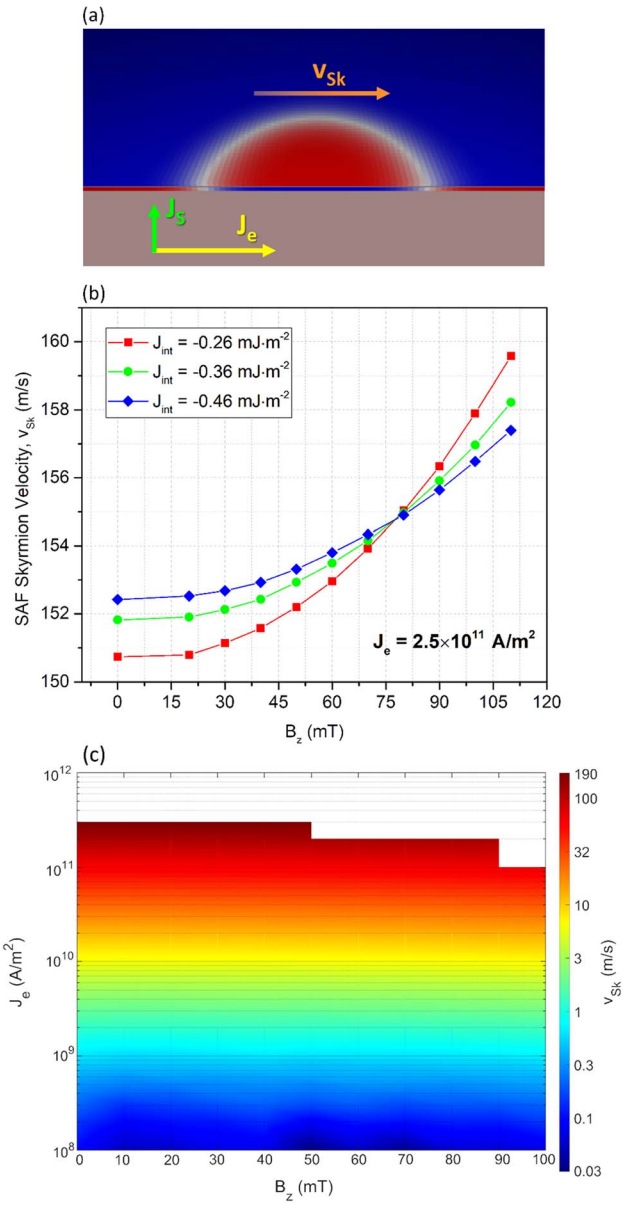

Fig. 5 Effect of extrinsic control parameters and interlayer exchange (ILE) coupling strength on the SAF skyrmion velocities. (a) Visualization of the calculated SAF skyrmion pair driven under current. (b) B_z dependence of the velocity of the SAF skyrmion pair for different ILE strengths at applied current density $J_e = 2.5 \times 10^{11}$ A m^{-2}. (c) Velocity of SAF skyrmion pair as a function of driving current density J_e and applied field B_z at $J_{int} = -0.13$ mJ m^{-2}.

fields. At this critical value of B_z, the coupling between the skyrmions and the skyrmion cores is expected to be affected by the polarizing field, and this is observed in Fig. 4(b). J_{int} proves to play a role in the translational motion of the skyrmion as larger ILE strength could provide stronger stability against the current pushing the skyrmion. For magnitudes below the decoupling field limits shown in Fig. 4(b), higher B_z leads to greater velocity when current is applied.

To elucidate the effect of the applied current density in different driving regimes of the SAF skyrmions, we present the current density–skyrmion pair velocity-B_z field phase diagram in Fig. 5(c). The phase diagram ends at high current densities due to the decoupling of the top and bottom skyrmions (white region). The skyrmion decoupling current decreases with the increase in the field B_z. This effect is due to breakdown of the coupling under larger magnetic fields under reduced symmetry as mentioned in Fig. 4(b). The maximum velocity reached for this system is about 196 m s^{-1} at the lower field. On the other hand, the lower limit for J_e that can still drive the SAF skyrmion adiabatically (0.04 m s^{-1}) is observed on the order of 1×10^8 A m^{-2}. As power dissipation scales quadratically with the applied current density, adiabatic skyrmion velocities might be identified as an ultra-low power skyrmion driving regime.

At the lowest current density limit (10^8 A m^{-1}, 0.03 m s^{-1} SAF skyrmion velocity), the operation time to move an SAF skyrmion of 20 nm diameter across a 20 nm distance at this velocity is around 0.7 μs. The operation rate is therefore on the order of 1/(0.7 μs) = 1.43 MHz. This rate is already sufficient or an order

of magnitude higher than the standard data transfer interface rates such as those at the SPI (serial peripheral interface) and those in I2C commonly used by state-of-the-art sensors (*i.e.*, BMP581 Barometric Pressure Sensor[36] and BMI323 inertial measurement unit from Bosch Sensortec[37]). Therefore, despite the slow rate, many practical applications can be implemented with the SAF skyrmions. Our SAF skyrmion system's much lower power consumption with respect to microelectronics and its nonvolatile data processing characteristics provide significant potential advantages. For many embedded systems or Internet of things applications, GHz rates are not needed or even preferred because of the higher power consumption. Since not all technological applications need GHz rates, these small velocities should be fine also for the relevant niche applications like sensor nodes and networks. For sensor deployment and networks, power consumption can be the main figure of merit to be optimized and the information processing rate can be traded off to obtain low power consumption.

Temperature dependence, sidewall roughness, pinning sites and polycrystallinity typically hinder experimental realization of many of the useful properties of skyrmions. Despite their significance, very few computational or theoretical studies on skyrmions quantify these detrimental effects or provide guidance on how to overcome them.[38,39] Increasing temperature in the SAF multilayer from 0 K to 100 K blurs the skyrmion borders and diminishes their stability (Fig. S1 in the ESI†). For the same SAF skyrmion multilayer configuration, a slight increase of uniaxial anisotropy K_u from 85×10^4 J m^{-3} to 95×10^4 J m^{-3} at 100 K offsets the random temperature fluctuations and restores the 0 K-like stability. The applied external field, however, cannot provide the same stabilizing effect as K_u since the field contributes Zeeman terms with opposite signs at the coupled skyrmion interfaces (Fig. S2 in the ESI†). Uniaxial anisotropy variations have been found to profoundly affect SAF skyrmion pairing and current-driven motion (Fig. S5 and S6 in the ESI†), where a random change of 5% or more of the nominal uniaxial anisotropy ($K_u^* = K_u^0 + \Delta K$, where $\Delta K \sim \mathcal{N}(0,\ 5\% \times K_u^0)$) can hinder current-driven skyrmion propagation (Videos V1–V4 in the ESI†). In addition, 3° or more of off-axis misorientation of uniaxial anisotropy (*i.e.*, due to substrate miscuts) has been found to be sufficient to completely hinder current-driven skyrmion motion (Fig. S6 in Videos V5–V9 in the ESI†). Unlike temperature or uniaxial anisotropy, sidewall roughness does not prevent SAF skyrmion pairing or their paired current-driven motion (Fig. S7 and Videos V10–V13 in the ESI†) when the random sidewall roughness within $3\sigma \leq 60\%$ of the channel widths of SAF multilayer slabs can sustain coupled skyrmions and their propagation. These results emphasize the significance of temperature, the uniaxial anisotropy parameter, minimal substrate miscuts, and uniform and single crystal magnetic film quality for experimental demonstrations of skyrmion devices.

Discussion

Dependence of SAF skyrmion stability on material constants

The two coupled skyrmions along the two interfaces of the SAF trilayer are stabilized as a balance of the competing energy terms mentioned in eqn (2). Fig. 1 shows that the main driver of the coupled skyrmions is the uniaxial anisotropy energy (E_K), which also contains both magnetocrystalline (uniaxial) and demagnetizing (shape) anisotropy terms. After the uniaxial anisotropy energy, DM interaction E_{DMI} changes by more than an order magnitude within the radius range of 30 nm and contributes to the equilibrium configuration. The Heisenberg exchange interaction E_A, which is constant within each ferromagnetic layer, also helps equilibrate the SAF skyrmion at below a 30 nm radius. The interlayer exchange term, E_{ILE}, is about two orders of magnitude weaker than the other magnetic energy terms within the radius range of 5–30 nm. This term is too weak to participate substantially in the stabilization of the skyrmion radius within each layer. The main contribution of this term is in the antiferromagnetic coupling of the skyrmions on the opposite ends of the multilayer. Overall, for stabilizing the skyrmion radius, the main terms that contribute are E_K, E_{DMI}, and E_A. For coupling the skyrmions antiferromagnetically, E_{ILE} is the critical and unique term which does not exist in ferromagnetic skyrmion systems.

Comparison of our semi-analytical model and numerical micromagnetic LLG model

We modelled the equilibrium radii of the SAF skyrmions both using a semi-analytical model that we developed and the numerical LLG model. The details of both models are presented in the results and methods parts. The semi-analytical model is an approximation, but its closed form expressions allow for interpreting how these terms scale with the geometric or material parameters while micromagnetic LLG models do not allow for it. Thus, the competing driving forces and the prominent materials and geometric factors can be better understood. The results in Fig. 1 are based on both the semi-analytical model and the micromagnetic model, while the rest of the figures show results from the micromagnetic LLG models.

In eqn (2)–(8), the equilibrium radius and the domain wall width are the key parameters that both affect these energy terms and are also affected by these terms. Below is a term-by-term analysis of the equilibrated SAF skyrmion pairs:

Heisenberg exchange (E_A). This term, as described with eqn (3), scales with the exchange stiffness coefficient of the FM layers and the FM layer thicknesses. The skyrmion radius dependence of this term as shown in Fig. 1(b) indicates that this term contains at least two competing effects: larger skyrmion sizes cause stronger ferromagnetic coupling within the skyrmion. Below a 5 nm radius, this term shows strong repulsive effects due to the antiferromagnetic interactions within the layer. Thus, a lower limit to the skyrmion sizes is established.

Effective anisotropy (E_K). This term is described in eqn (4). The $\pi K d w^2$ coefficient acts as the energy term that contains the uniaxial and shape anisotropy densities scaled with thickness and the skyrmion's domain wall width w (or scaled with the domain wall volume). Uniaxial anisotropy is assumed to reorient the spins out of plane while the shape anisotropy competes with the uniaxial anisotropy term K_u to reorient the spins towards the film plane. Finally, the scale factor contains a linear

term and a subtractive exponentially decaying term. If the skyrmion grows indefinitely, E_K converges to a ferromagnetic-like behavior. The competition between the shape and the uniaxial anisotropy leads to a balance ($E_K \sim 0$) around a 1 nm radius when the strong demagnetizing fields offset the uniaxial term. The linear term originates from the overall spin orientation of the "infinitely" wide thin film. The exponential decaying term originates because of the skyrmion domain walls.

Dzyaloshinskii–Moriya interaction (E_{DMI}). This term, described in eqn (5), is oppositely signed with respect to the other terms. It scales with w instead of w^2 (which is the case for E_K). This term, together with the (Heisenberg) exchange stiffness, causes an equilibrium point to be established in the total magnetic anisotropy expression.

Interlayer exchange interaction (E_{ILE}). This term, described in eqn (6), captures the effect of interfacial antiferromagnetic coupling ($J_{int} < 0$) through the RKKY interaction. For a fixed material thickness and type, this term converges to an upper limit in the "infinitely" large skyrmion size limit as the exponent term in eqn (6) vanishes in the limit of large ρ. This upper limit is determined by the $J_{int}dw$ coefficient. The magnitude of this energy term is smaller than the others due to the small value of J_{int} and the multiplicative factor with the exponential terms.

Overall, M_{sat}, K_u, DMI constant D_{ind} and their contributions affect the stability of the SAF skyrmion the most. The increase in the uniaxial anisotropy of the system will allow the skyrmion to stabilize at larger radii. On the other hand, the interlayer exchange interaction has the lowest contribution to the total energy, which also implies that it has little effect on the skyrmion size. However, this term is crucial for maintaining the SAF skyrmion structure against externally applied conditions, such as the current density that moves the skyrmion in the structure. We observe that the equilibrium state of the SAF skyrmion at minimum total energy is attained at a radius of 20 nm, and we also obtain a close value by simulating the SAF skyrmion in MuMax3 with the same parameters. The MuMax3 micromagnetic model based on the LLG equation is described further in the Methods.

Since M_{sat}, K_u, and the DMI constant D_{ind} affect the skyrmion stability and sizes the most, Fig. 2 and 3 show the effect of these parameters in further detail. The skyrmion sizes generally increase linearly with increasing saturation magnetization of the ferromagnetic layers, but after a critical M_{sat}, the skyrmion sizes are dominated mainly by M_{sat}. Fig. 2(a) shows that the equilibrium coupled SAF skyrmion sizes are below 15 nm in radius for $M_{sat} < 930$ kA m^{-1}. For M_{sat} beyond this threshold, the equilibrium skyrmion radii increase exponentially.

The effects of the uniaxial anisotropy constant and saturation magnetization on the equilibrium coupled SAF skyrmion radii are shown in the phase diagram in Fig. 2(b). For a constant M_{sat}, higher K_u shrinks the skyrmion radius, since the skyrmion minimizes its energy with a smaller total uniaxial anisotropy and demagnetizing energy term. Greater M_{sat} for a constant K_u increases the equilibrium skyrmion radii since the larger demagnetizing fields with higher magnetization minimize the total energy when the skyrmion radius is larger. The skyrmion radius can be changed from 1.25 nm to 38 nm due to the total effective magnetic energy expression formed with the different uniaxial anisotropy and the saturation magnetization values, as shown in the color shaded region. The white region of the phase diagram with high M_{sat} and low K_u (below 10^6 J m^{-3}) shows the stabilization of labyrinth domain structures and here, skyrmions are no longer supported. In the gray-shaded region, no results are reported since the cell sizes of the simulations become comparable to the lattice constants. Around these cell sizes, the micromagnetic assumption of homogeneous micromagnetic cell approximation no longer applies to the discrete atomic spins. Thus, the phase diagram excludes the gray region. These results show that the balance of M_{sat} and K_u establishes the equilibrium size of the coupled SAF skyrmions.

The FM/NM/FM layer has mirror symmetry in its geometry, but the DMI constant of both interfaces is an important parameter that can preserve or break the topology and chirality of the skyrmion. As a result, large D_{ind} values at the interfaces break the symmetry and cause labyrinth structures to form, as shown in the upper white regions of Fig. 3. In the low D_{ind} and higher K_u cases, as shown in the gray region of the phase diagram, the skyrmion sizes fall below the lower cell size thresholds for micromagnetic models to be valid. Below 1.25 nm, atomically small domain features can no longer be captured by micromagnetic models, and therefore, no results are reported in that region of the phase diagram. For a constant D_{ind} constant, larger uniaxial anisotropy tends to shrink the skyrmion sizes due to the positive sign of the anisotropy constant that would minimize the total energy only if the skyrmion becomes smaller. The formation of a stable skyrmion window and the opposing effects of D_{ind} and K_u on the skyrmion sizes indicates the competition of uniaxial anisotropy and Dzyaloshinskii–Moriya interaction.

The effect of interlayer exchange (ILE) and an external magnetic field have been investigated as shown in Fig. 4. The top and bottom skyrmions are coupled to each other through the ILE term. In Fig. 4(a), increasing the B_z enlarges the top skyrmion while it tries to shrink the bottom skyrmion. The ILE can no longer keep the top and bottom layer skyrmions perfectly aligned since the core of the top skyrmion ($+z$) expands and overcomes the AFM coupling. The difference is observed at $B_z = 100$ mT.

In Fig. 4(b), the ILE interaction constant J_{int} with a higher magnitude keeps the top and bottom skyrmions tightly bound with similar radii especially for low B_z fields. Increasing the external field reduces the coupling without complete detachment. For weak ILE constants, any external magnetic field B_z is going to cause a significant radius difference. Fig. S3 in the ESI† includes further details on the effect of J_{int} and B_z on the skyrmion radius of the bottom interface. While the external field can cause the detachment of the SAF skyrmions above a critical field threshold, the SAF skyrmion velocity is not significantly affected by the external magnetic field. The driving force for exponential increase in skyrmion velocity is the applied current density, as shown in Fig. 5(b) and (c).

Although the same parameters reported in ref. 35 are used, our study is fundamentally different from the earlier skyrmion investigations in terms of the purpose, methods, and the results. Different from ref. 35 and similar skyrmion investigations, our study has three unique aspects. First, our study presents a semi-analytical model, which helped identify the

key driving forces and anisotropy fields and this model was used in the supplementary section to overcome temperature effects (ESI Fig. S1†). Second, our study shows the effects of changing the key material parameters (saturation magnetization, uniaxial anisotropy, DMI parameter, and interlayer exchange) and the external magnetic field on the skyrmion and skyrmion pair stability. Third, our study shows the effects of imperfections on the device operation for the first time for SAF skyrmions. The effects of different material parameters due to fabrication imperfections (Fig. 2–5), sidewall roughness, substrate miscuts or crystalline misorientation and finite temperature effects on device performance are analyzed and discussed (ESI†). We also proposed ways to overcome finite temperature effects using uniaxial anisotropy (ESI†). Different from earlier studies, we analyzed SAF skyrmion propagation from a power consumption standpoint and focused on skyrmions, not domain-like micron-scale bubbles as in previous studies.[35] Each of these effects is too hard or impossible to test experimentally. Therefore, our computational study helped elucidate the key driving anisotropy field forces and regimes that would not otherwise be identified, and new insights are obtained through our models.

SAF skyrmions could be explored in new 2D semiconducting $NbSi_2N_4$, VSi_2N_4, and VSi_2P_4 with near or above room temperature magnetism. Since the magnetic easy axis of VSi_2N_4 can be tuned from in-plane to out-of-plane by applying tensile biaxial strain or electron doping,[40] these new 2D magnetic semiconductors could be explored for SAF skyrmion demonstrations. Their nontrivial topological properties, 2D ferromagnetism, Ising superconductivity, and valley polarization also make these spin gapless semiconductors and bipolar magnetic semiconductors interesting candidates for topological magnetotransport studies.[41,42] Interfacial DMI is increased for monolayer or very thin magnetic films and this effect can be beneficial for making nanometer scale SAF spintronic devices.[43] Implementing SAF skyrmions in such 2D materials with higher Curie temperatures might be a fruitful future research direction.

To conclude, we investigated the theory of SAF skyrmions and the stability conditions that allow for their applications in logic and memory-based devices. The theory of SAF skyrmions helped elucidate new insights into which terms prominently contribute to the equilibrium and propagation of these coupled skyrmions. Further investigation into the effect of an external vertical magnetic bias field and the current density revealed that SAF skyrmions can reach ~200 m s^{-1} without the THE. The SAF velocities are an order of magnitude higher than those of the typical ferromagnetic skyrmions. Skyrmion drive current densities could be reduced to as low as 10^8 A m^{-2} and a more than 3 orders of magnitude-wide window of current densities can be feasible for stable, fast, and THE-free skyrmion propagation. The reduction in current density could quadratically reduce Joule heating by as much as 6 orders of magnitude. Furthermore, the models emphasized the significance of temperature, the uniaxial anisotropy parameter, minimal substrate miscuts, and uniform and single crystal magnetic film quality for experimental demonstrations of skyrmion devices. These results complete the theory of SAF skyrmions and pave the way to experimental demonstrations of THE-free SAF interfaces with improved equilibrium, dynamics, and power savings.

Methods

Micromagnetic model of the SAF skyrmion system

The SAF structure shown in Fig. 1(a) consists of two ferromagnetic (FM) layers and a nonmagnetic (NM) layer is in between. The antiferromagnetically (AFM) coupled top and bottom layers in the synthetic antiferromagnetic (SAF) system were modelled using the MuMax3 micromagnetic solver.[28] This software solves the Landau–Lifshitz–Gilbert (LLG) equation using the finite-difference method.

$$\frac{\partial \mathbf{m}}{\partial t} = -|\gamma|\mathbf{m} \times \mathbf{H}_{\mathbf{eff}} + \alpha \mathbf{m} \times \frac{\partial \mathbf{m}}{\partial t} \quad (9)$$

where $\gamma = 1.76 \times 10^{11}$ A s kg^{-1} is the gyromagnetic ratio and $\mathbf{H}_{\mathbf{eff}}$ is the effective field. The LLG equation above consists of two main terms: the first term describes the magnetization precession in the presence of $\mathbf{H}_{\mathbf{eff}}$ and the second term captures damping motion of the unit magnetic moment $\mathbf{m}$. The effective field $\mathbf{H}_{\mathbf{eff}}$ is the functional derivative of the total magnetic anisotropy energy density E_{tot} (defined in eqn (2)) of the magnetic system with respect to $\mathbf{m}$ and is defined as:

$$\mathbf{H}_{\mathbf{eff}} = -\frac{1}{\mu_0 M_{\mathrm{s}}} \frac{\delta E_{\mathrm{tot}}}{\delta \mathbf{m}} \quad (10)$$

The geometry and parameters were set according to the (Co/CoFeB)/Ir/(Co/CoFeB) (FM/NM/FM) system.[35] The following parameters are used in the calculations (unless otherwise mentioned): $M_{\mathrm{sat}} = 954 \times 10^3$ A m^{-1}, $A = 10 \times 10^{-12}$ J m^{-1}, $K_{\mathrm{u}} = 0.85 \times 10^6$ J m^{-3}, $D_{\mathrm{ind}} = 2.0 \times 10^{-3}$ J m^{-2}, and $\alpha = 0.1$. The structure in the simulation ($512 \times 512 \times 2$ nm^3) consisted of two FM layers (each has a thickness of 1 nm), while the NM layer was not explicitly included and instead the interlayer exchange constant was scaled to a RKKY value of -0.13×10^{-3} J m^{-2} for a given thickness of the NM layer of 1 nm. The cell size was set to $c_x = 1$ nm, $c_y = 1$ nm, and $c_z = 1$ nm. For the phase diagrams, the sweeps on MuMax3 were done for the cell size $c_x = c_y = 0.25$ nm to obtain the minimum skyrmion radius range in the micromagnetic limits, both cell size values chosen in-plane yield the same results (see Fig. S4 in the ESI† for $c_x = c_y = 1$ nm).

For the dynamic simulations of the SAF skyrmion we used SOT-driven current in the SAF structure. We applied the current density in the CPP configuration so that the SAF skyrmion could move in the in-plane direction (+x) and the spin hall angle θ_{Hall} was set to + 0.25. The LLG equation including the SOT term then becomes:

$$\frac{\partial \mathbf{m}}{\partial t} = -|\gamma|\mathbf{m} \times \left(\mathbf{H}_{\mathbf{eff}} + a_{\mathrm{j}}(\mathbf{m} \times \mathbf{p}) + b_{\mathrm{j}}\mathbf{p}\right) + \alpha \mathbf{m} \times \frac{\partial \mathbf{m}}{\partial t}, \quad (11)$$

where the perfectors a_{j} and b_{j} are the field strengths of the damping-like and field-like torques, respectively. $\mathbf{p}$ is the polarization unit vector in the direction of the magnetic moments that are injected into the FM layer and is given by $\mathbf{p} = \mathrm{sign}(\theta_{\mathrm{Hall}}) j \times n = -\hat{y}$, where the current direction $\mathbf{j} = \hat{x}$ and the surface normal of the heavy metal layer $n = \hat{z}$.

Interlayer exchange energy functional

The interlayer exchange coupling (RKKY) energy in the SAF multilayer system[34] is defined as

$$E_{\mathrm{ILE}} = -J_{\mathrm{int}}(\cos\theta_1\cos\theta_2 + \sin\theta_1\sin\theta_2\cos(\varphi_1 - \varphi_1)),$$

where θ_i and φ_i are the polar and the azimuthal angles of the skyrmion domain wall, respectively. The subscripts 1 and 2 refer to the top and bottom skyrmions, respectively.

$\varphi_2 = \varphi_1 + \pi$ and $\theta_2 = \theta_1 + \pi$ for the Néel type of skyrmion pairs shown in Fig. 1(a), and then E_{ILE} reduces to

$$E_{\mathrm{ILE}} = -J_{\mathrm{int}}(\cos(2\theta_1 - \pi)),$$

Using the definition of θ from ref. 27 and integrating with respect to the ratio term ϱ we finally present the energy as the following approximated expression,

$$\begin{aligned} E_{\mathrm{ILE}} &= -J_{\mathrm{int}}\int_0^{\infty}\cos\left(4\ \tan^{-1}\frac{\sinh\rho}{\sinh\varrho} - \pi\right)d\varrho \\ &= -2\pi J_{\mathrm{int}}dw\left(5.005 - 2.149\ \mathrm{e}^{-0.93\rho}\right), \end{aligned}$$

where d and w are the layer thickness and the skyrmion domain wall width, respectively.

Data availability

Data supporting the findings of this study are available within the article and its ESI† and from the corresponding authors upon request. Source data are provided with this paper and in the link: … (link to be provided if requested by the reviewers or the journal after acceptance).

Author contributions

M. C. O. conceived and coordinated the project. R. Y. performed most of the micromagnetic simulations with support from A. M. C. M. C. O. and R. Y. interpreted the results and prepared the manuscript. All authors commented on the manuscript.

Conflicts of interest

The authors declare no competing interests.

Acknowledgements

This study has been funded by the European Research Council (ERC) Starting Grant SKYNOLIMIT Grant No. 948063, ERC Proof of Concept Grant SuperPHOTON Grant No. 101100718 and partially from TÜBİTAK Grant No. 120F230.

References

1 Y. Tokura and N. Kanazawa, *Chem. Rev.*, 2021, **121**, 2857–2897.
2 A. Fert, N. Reyren and V. Cros, *Nat. Rev. Mater.*, 2017, **2**, 17031.
3 N. D. Khanh, T. Nakajima, X. Yu, S. Gao, K. Shibata, M. Hirschberger, Y. Yamasaki, H. Sagayama, H. Nakao, L. Peng, K. Nakajima, R. Takagi, T.-h. Arima, Y. Tokura and S. Seki, *Nat. Nanotechnol.*, 2020, **15**, 444–449.
4 N. Kanazawa, S. Seki and Y. Tokura, *Adv. Mater.*, 2017, **29**, 1603227.
5 N. Gao, S. G. Je, M. Y. Im, J. W. Choi, M. Yang, Q. Li, T. Y. Wang, S. Lee, H. S. Han, K. S. Lee, W. Chao, C. Hwang, J. Li and Z. Q. Qiu, *Nat. Commun.*, 2019, **10**, 5603.
6 G. Yang, P. Stano, J. Klinovaja and D. Loss, *Phys. Rev. B*, 2016, **93**, 224505.
7 Y. Wu, S. Zhang, J. Zhang, W. Wang, Y. L. Zhu, J. Hu, G. Yin, K. Wong, C. Fang, C. Wan, X. Han, Q. Shao, T. Taniguchi, K. Watanabe, J. Zang, Z. Mao, X. Zhang and K. L. Wang, *Nat. Commun.*, 2020, **11**, 3860.
8 K. Huang, D.-F. Shao and E. Y. Tsymbal, *Nano Lett.*, 2022, **22**, 3349–3355.
9 B. Dieny, I. L. Prejbeanu, K. Garello, P. Gambardella, P. Freitas, R. Lehndorff, W. Raberg, U. Ebels, S. O. Demokritov, J. Akerman, A. Deac, P. Pirro, C. Adelmann, A. Anane, A. V. Chumak, A. Hirohata, S. Mangin, S. O. Valenzuela, M. C. Onbaşlı, M. D'Aquino, G. Prenat, G. Finocchio, L. Lopez-Diaz, R. Chantrell, O. Chubykalo-Fesenko and P. Bortolotti, *Nat. Electron.*, 2020, **3**, 446–459.
10 X. Zhang, Y. Zhou, K. Mee Song, T.-E. Park, J. Xia, M. Ezawa, X. Liu, W. Zhao, G. Zhao and S. Woo, *J. Phys.: Condens. Matter*, 2020, **32**, 143001.
11 R. Juge, N. Sisodia, J. U. Larrañaga, Q. Zhang, V. T. Pham, K. G. Rana, B. Sarpi, N. Mille, S. Stanescu, R. Belkhou, M.-A. Mawass, N. Novakovic-Marinkovic, F. Kronast, M. Weigand, J. Gräfe, S. Wintz, S. Finizio, J. Raabe, L. Aballe, M. Foerster, M. Belmeguenai, L. D. Buda-Prejbeanu, J. Pelloux-Prayer, J. M. Shaw, H. T. Nembach, L. Ranno, G. Gaudin and O. Boulle, *Nat. Commun.*, 2022, **13**, 4807.
12 W. Legrand, D. Maccariello, F. Ajejas, S. Collin, A. Vecchiola, K. Bouzehouane, N. Reyren, V. Cros and A. Fert, *Nat. Mater.*, 2020, **19**, 34–42.
13 H. Wang, Y. Liu, P. Wu, W. Hou, Y. Jiang, X. Li, C. Pandey, D. Chen, Q. Yang, H. Wang, D. Wei, N. Lei, W. Kang, L. Wen, T. Nie, W. Zhao and K. L. Wang, *ACS Nano*, 2020, **14**, 10045–10053.
14 G. Yu, P. Upadhyaya, X. Li, W. Li, S. K. Kim, Y. Fan, K. L. Wong, Y. Tserkovnyak, P. K. Amiri and K. L. Wang, *Nano Lett.*, 2016, **16**, 1981–1988.
15 X. Zhang, Y. Zhou and M. Ezawa, *Nat. Commun.*, 2016, **7**, 10293.
16 S. Luo and L. You, *APL Mater.*, 2021, **9**, 050901.
17 L. Gnoli, F. Riente, M. Vacca, M. Ruo Roch and M. Graziano, *Electronics*, 2021, **10**, 155.
18 R. A. Duine, K.-J. Lee, S. S. P. Parkin and M. D. Stiles, *Nat. Phys.*, 2018, **14**, 217–219.
19 J. Xia, X. Zhang, K.-Y. Mak, M. Ezawa, O. A. Tretiakov, Y. Zhou, G. Zhao and X. Liu, *Phys. Rev. B*, 2021, **103**, 174408.
20 X. Zhang, Y. Zhou and M. Ezawa, *Sci. Rep.*, 2016, **6**, 24795.

21 A. Fernández-Pacheco, E. Vedmedenko, F. Ummelen, R. Mansell, D. Petit and R. P. Cowburn, *Nat. Mater.*, 2019, **18**, 679–684.
22 S. Krishnia, P. Sethi, W. L. Gan, F. N. Kholid, I. Purnama, M. Ramu, T. S. Herng, J. Ding and W. S. Lew, *Sci. Rep.*, 2017, **7**, 11715.
23 A. G. Kolesnikov, M. E. Stebliy, A. S. Samardak and A. V. Ognev, *Sci. Rep.*, 2018, **8**, 16966.
24 S. Qiu, J. Liu, Y. Chen, X. Qi and L. Fang, *J. Magn. Magn. Mater.*, 2022, **554**, 169144.
25 R. Tomasello, V. Puliafito, E. Martinez, A. Manchon, M. Ricci, M. Carpentieri and G. Finocchio, *J. Phys. D: Appl. Phys.*, 2017, **50**, 325302.
26 X. S. Wang, H. Y. Yuan and X. R. Wang, *Commun. Phys.*, 2018, **1**, 31.
27 F. Büttner, I. Lemesh and G. S. D. Beach, *Sci. Rep.*, 2018, **8**, 4464.
28 A. Vansteenkiste, J. Leliaert, M. Dvornik, M. Helsen, F. Garcia-Sanchez and B. V. Waeyenberge, *AIP Adv.*, 2014, **4**, 107133.
29 S. Woo, K. M. Song, X. Zhang, Y. Zhou, M. Ezawa, X. Liu, S. Finizio, J. Raabe, N. J. Lee, S.-I. Kim, S.-Y. Park, Y. Kim, J.-Y. Kim, D. Lee, O. Lee, J. W. Choi, B.-C. Min, H. C. Koo and J. Chang, *Nat. Commun.*, 2018, **9**, 959.
30 J. Sampaio, V. Cros, S. Rohart, A. Thiaville and A. Fert, *Nat. Nanotechnol.*, 2013, **8**, 839–844.
31 G. P. Fuentes, J. Holanda, Y. Guerra, D. B. O. Silva, B. V. M. Farias and E. Padrón-Hernández, *J. Magn. Magn. Mater.*, 2017, **423**, 262–266.
32 J. Weissmüller, A. Michels, J. G. Barker, A. Wiedenmann, U. Erb and R. D. Shull, *Phys. Rev. B: Condens. Matter Mater. Phys.*, 2001, **63**, 214414.
33 H.-B. Braun, *Phys. Rev. B: Condens. Matter Mater. Phys.*, 1994, **50**, 16485–16500.
34 Z. Zhang, L. Zhou, P. E. Wigen and K. Ounadjela, *Phys. Rev. B: Condens. Matter Mater. Phys.*, 1994, **50**, 6094–6112.
35 T. Dohi, S. Duttagupta, S. Fukami and H. Ohno, *Nat. Commun.*, 2019, **10**, 5153.
36 B. Sensortec, *BMP581 Barometric Pressure Sensor Datasheet, B. Sensortec Report BST-BMP581-DS004*, Bosch Sensortec, 2023.
37 B. Sensortec, *BMI323 Small, Versatile 6DoF Sensor Module Datasheet, Report BST-BMI323-DS000-09*, Bosch Sensortec, 2023.
38 A. M. Cheghabouri and M. C. Onbasli, *Sci. Rep.*, 2019, **9**, 9496.
39 A. Mousavi Cheghabouri, F. Katmis and M. C. Onbasli, *Phys. Rev. B*, 2022, **105**, 054411.
40 M. R. K. Akanda and R. K. Lake, *Appl. Phys. Lett.*, 2021, **119**, 052402.
41 Y. Feng, Z. Wang, X. Zuo and G. Gao, *Appl. Phys. Lett.*, 2022, **120**, 092405.
42 Q. Cui, Y. Zhu, J. Liang, P. Cui and H. Yang, *Phys. Rev. B*, 2021, **103**, 085421.
43 M. R. K. Akanda, I. J. Park and R. K. Lake, *Phys. Rev. B*, 2020, **102**, 224414.